Supplemental Material for "Three-Dimensional Wiring for Extensible Quantum Computing: The Quantum Socket"

J. H. Béjanin,[1,2,*] T. G. McConkey,[1,3,*] J. R. Rinehart,[1,2] C. T. Earnest,[1,2] C.R. H. McRae,[1,2] D. Shiri,[1,2,†] J. D. Bateman,[1,2,‡] Y. Rohanizadegan,[1,2] B. Penava,[4] P. Breul,[4] S. Royak,[4] M. Zapatka,[5] A. G. Fowler,[6] and M. Mariantoni[1,2,§]

[1]*Institute for Quantum Computing, University of Waterloo, 200 University Avenue West, Waterloo, Ontario N2L 3G1, Canada*
[2]*Department of Physics and Astronomy, University of Waterloo, 200 University Avenue West, Waterloo, Ontario N2L 3G1, Canada*
[3]*Department of Electrical and Computer Engineering, University of Waterloo, 200 University Avenue West, Waterloo, Ontario N2L 3G1, Canada*
[4]*INGUN Prüfmittelbau GmbH, Max-Stromeyer-Straße 162, D-78467 Konstanz, Germany*
[5]*INGUN USA, Inc., 252 Latitude Lane, Suite 102, Lake Wylie, South Carolina 29710-8152, USA*
[6]*Google, Inc., Santa Barbara, California 93117, USA*

(Dated: August 7, 2016)

In this Supplemental Material, we describe the various experimental setups and settings used for the measurements reported in the main text; additionally, we give further details about the microwave simulations of the quantum socket, the S-parameter characterization, the resonator measurements, as well as the spring tests. Furthermore, we introduce an extended version of the surface code architecture introduced in the main text and, finally, we show a set of microwave pulse tests.

PACS numbers: 03.67.Lx, 06.60.Ei, 85.40.Ls, 85.25.-j
Keywords: Quantum Computing; Scalable Qubit Architectures; Quantum Socket; Three-Dimensional Wires; Microwave Interconnects; Superconducting Quantum Circuits; Quantum Error Correction

S1. INTRODUCTION

This Supplemental Material is organized as follows. In Sec. S2, we describe the experimental setups and settings utilized to perform the implementation and characterization of the quantum socket as well as the resonator measurements reported in the main text. In Sec. S3, we show a set of simulated electric field animations. In Sec. S4, we characterize the microwave anomaly due to the screw-in micro connector. In Sec. S5, we discuss in detail the geometry of the coupling region between a CPW transmission line and a superconducting resonator; additionally, we show the fit required to extract the internal quality factor of the resonators. In Sec. S6, we present a movie of the cryogenic spring tests. In Sec. S7, we show a possible extension of the surface code architecture proposed in Sec. VI of the main text, where two readout resonators per qubit are used. Finally, in Sec. S8, we present a brief study of the quantum socket behavior when fast microwave pulses are applied, corroborating the dispersion results in Appendix G of the main text.

S2. EXPERIMENTAL SETUPS AND SETTINGS

The various experimental setups and settings will be introduced following the same order as the sections and subsections in the main text.

SIII. IMPLEMENTATION

All the main parts of the microwave package, i.e., the lid, washer, and sample holder, were made from high-purity Al alloy 5N5 (99.9995 % purity) provided by Laurand Associates, Inc. The very low level of impurities in this alloy assures minimal stray magnetic fields generated by the package itself, as confirmed by the magnetic tests discussed in Appendix B of the main text. All parts of the package holder assembly (including the package holder horizontal plate and the horizontal mounting plate) were made from high thermal conductivity C10100 oxygen-free electrolytic (OFE) copper alloy, with a residual-resistivity ratio larger than 300. The parts were polished to a mirror finish before being gold plated. No Ni adhesion underlayer and an Au bath with minimum magnetic impurities were used. The deposited Au was hard Au, type I, grade C (MIL-G-45204C), with a total measured quantity of Ni, iron, and cobalt of 0.204 %.

The three-dimensional wires are torqued into the 2.5 mm thread in the package's lid by means of the grooves partially visible on the bottom of Fig. 4 (a) in the main text. The screw-in micro connector features similar grooves for torquing into the back end of the wire (cf. main text, Fig. 4 (c)).

* These two authors contributed equally to this work.
† Department of Physics, Chalmers University of Technology, SE-412 96 Göteborg, Sweden.
‡ Present address: The Edward S. Rogers Sr. Department of Electrical and Computer Engineering, University of Toronto, 10 King's College Road, Toronto, Ontario M5S 3G4, Canada.
§ Corresponding author: matteo.mariantoni@uwaterloo.ca

The washer's springs are glued to the four recesses in the lid of the microwave package by way of Vibra-Tite 12110 from ND Industries, Inc. This thread locker was tested several times in the DR at $\sim$10 mK, exhibiting a very good performance and durability.

The coaxial cables between the screw-in micro connectors and the SMP connectors on the horizontal plate of the package holder are from the EZ Form Cable Corporation, model EZ 47-CU-TP (EZ 47). The SMP connectors, also from EZ Form, are models SMP bulkhead jack for 0.047 inch coaxial cables (SMP 047; installed in the package holder horizontal plate) and SMP bulkhead plug with limited detent for 0.086 inch cables (SMP 086; installed in the horizontal mounting plate attached to the MC stage of the DR). All SMP connectors were custom-made non-magnetic connectors.

SD. Alignment

The dark field images displayed in Fig. 5 of the main text were taken with an Olympus MX61 microscope at $\times$5 magnification, manual exposure, and $\sim$500 ms exposure time. Before imaging, the samples were cleaned for a few seconds in a bath of isopropyl alcohol with ultrasounds.

The resistances reported in Table II of the main text were probed by means of a multimeter from the Fluke Corporation, model 289. In a few instances, the resistance values were confirmed using a precision source-measure unit from Keysight Technologies Inc., model B2911A.

SIV. CHARACTERIZATION

SA. Four-point measurements

In the setup used for the four-point measurements, the package was attached to the MC stage of the DR and connected to a set of phosphor bronze twisted pairs from Lake Shore Cryotronics, Inc., with gauge AWG 32 from room temperature to 3 K and AWG 36 from 3 K to 10 mK. The twisted pairs were thermally anchored at all DR stages and connected at room temperature to a precision source-measure unit from Keysight, model B2911A. In the I-V characteristic curve of Fig. 6 in the main text, the voltage measurements were delayed by 5 ms and averaged over 50 ms. The displayed data is averaged over 100 sweeps.

Assuming the largest bias current of $\sim$500 µA typically used in superconducting qubit experiments [1], a contact resistance of 150 mΩ would correspond to a dissipated power of less than 4 µW for a lattice of 100 qubits; this is significantly less than the available cooling power of any standard DR operated at 20 mK. However, any even small local heating could deteriorate the qubit performance and, thus, it is certainly desirable to reduce the wires' contact resistance.

SB. Two-port scattering parameters

The DUT in the inset of Fig. 7 (a) in the main text comprises a cable assembly attached to a three-dimensional wire by means of a screw-in micro connector. The cable assembly is made of an approximately 230 mm long semi-rigid coaxial cable EZ 47, which is soldered to an EZ Form custom-made SMA male connector, model 705538-347. The other end of the coaxial cable is soldered to the screw-in micro connector. The SMA connector of the DUT is connected to one port of a VNA from Keysight, model PNA-L N5230A by means of a flexible coaxial cable. The bottom interface of the wire is connected to a 2.92 mm end launch connector from Southwest Microwave, Inc., model 1092-01A-5, which then connects to the other port of the VNA through a second flexible coaxial cable. The 2.92 mm adapter is characterized by a flush coaxial back plane.

In order to measure the S-parameters of the DUT in the inset of Fig. 7 (a) in the main text, a two-tier calibration was performed. First, a two-port electronic calibration module (ECal) from Keysight, model N4691B, with 2.92 mm male connectors was used to set the measurement planes to the end of the flexible cables closer to the DUT. Second, a port-extension routine was performed to correct for the insertion loss, phase, and delay of the 2.92 mm adapter. This made it possible to set the measurement planes to the ports of the DUT.

The setup in Fig. 8 of the main text comprises a VNA from Keysight, model PNA-X N5242A, with ports 1 and 2 connected to a pair of flexible coaxial cables from Huber+Suhner AG, model SucoFlex 104-PE (with SMA male connectors). In order to calibrate the measurement, the flexible cables were first connected to a two-port ECal module from Keysight, model N4691-60006, featuring 3.5 mm female connectors. Unless specified, all calibrations were performed using SMA female to 3.5 mm male adapters. These adapters introduced negligible calibration errors from DC to 10 GHz. The flexible cables were then connected to the SMA female bulkhead adapter at the input and output ports of the DUT shown in Fig. 8. The DUT is similar to the microwave package and package holder shown in Fig. 4 (c) of the main text. However, for the characterization measurements the SMP adapters were substituted by SMA female-female bulkhead adapters. One of the EZ cables in the DUT is 228 mm long and the other is 232 mm long; the longer cable (output) is connected directly to the SMA bulkhead adapter, whereas the shorter cable (input) is prolonged using an SMA female-male adapter and, then, connected to the bulkhead adapter. These bulkhead adapters are the reference planes ii and xii associated with the input and output ports of the DUT, respectively, as shown in Fig. 8 of the main text.

In the two-port S-parameter measurements shown in Figs. 9 and 10 of the main text, we selected an intermediate frequency (IF) bandwidth $\Delta f_{\rm IF} = 500\,{\rm Hz}$, a constant excitation power $P_{\rm RF} = 0$ dB-milliwatts (dBm), and $N_{\rm RF} = 12001$ or $N_{\rm RF} = 100001$ measurement points for the Au and Ag samples, respectively. Note that the Ag measurements were performed without using the SMA female to 3.5 mm male adapters.

SC. Time-domain reflectometry

For the TDR measurements in Figs. 11 and 12 of the main text, the DUT is that in Fig. 8, though including the SucoFlex flexible coaxial cables. Thus, these cables were not calibrated out from the measurements. In particular, the TDR measurements referring to the input port of the DUT include a 2.0 m flexible cable.

The TDR sampling oscilloscope is from Teledyne LeCroy, model WaveExpert 100H; the oscilloscope features an electrical sampling module with 20 GHz bandwidth and a TDR step generator, model ST-20. The generated signal is a voltage square wave characterized by a nominal pulse rise time of 20 ps, amplitude of 250 mV, pulse width of 300 ns, and pulse repetition rate of 1 MHz.

SD. Signal crosstalk

The four-port calibration and measurement of the DUT were conducted by means of the ECal module N4691-60006 and PNA-X N5242A. We selected a frequency range from 10 MHz to 10 GHz, $\Delta f_{\rm IF} = 1\,{\rm kHz}$, $P_{\rm RF} = 0$ dBm, and $N_{\rm RF} = 64001$.

SV. APPLICATIONS TO SUPERCONDUCTING RESONATORS

The experimental setup used to measure the superconducting CPW resonators is shown in Fig. S1. The low-temperature system is a cryogen-free DR from BlueFors Cryogenics Ltd., model BF-LD250. The DR comprises five main temperature stages, where microwave components and samples can be thermally anchored: The RT, 50 K, 3 K, still (∼800 mK), cold plate (CP; ∼50 mK), and MC stage. We will describe the setup following the input signal through the various temperature stages, from port 1 to the input port of the microwave package (where the resonator sample is mounted) and from the output port of the package to port 2. The two ports are connected to the PNA-X N5242A, which serves as both the microwave source and readout apparatus. Port 1 is connected to the RT stage of the DR with SucoFlex flexible cables followed by a series of two semi-rigid coaxial cables from EZ Form, model EZ 86-Cu-TP/M17 (each approximately 1.2 m long, with silver-coated copper center conductor, solid PTFE dielectric, and tin-plated seamless copper outer conductor). Except for the PNA-X ports, which feature 3.5 mm connectors, all the connectors and bulkhead adapters are SMA type. In particular, the RT stage of the DR features a set of hermetic SMA bulkhead adapters from Huber+Suhner, model 34_SMA-50-0-3/111_N, with a tested leak rate for helium-4 lower than $1 \times 10^{-9}\,{\rm mbar\,l\,s^{-1}}$.

The DR stages, all the way to the MC stage, are connected by the series of five semi-rigid coaxial cables from Coax Co., Ltd., model SC-219/50-SS-SS (with stainless steel (SUS304) center and outer conductor and solid PTFE dielectric; the cable lengths from RT to MC are: 39.6 cm, 48.0 cm, 39.9 cm, 27.4 cm, and 20.0 cm, respectively). The cables are thermalized to the DR stages by way of cryogenic attenuators from the XMA Corporation-Omni Spectra®, model 2082-6418-XX-CRYO, where XX is the attenuation level in dB; for each stage between RT and MC, we chose XX = 03, 06, 06, 20, and 20, respectively. The input signals are filtered by means of a low-pass filter from Marki Microwave, Inc., model FLP-0960-2S, with bandpass from DC to 9.6 GHz. The filter is heat sunk at the MC stage by anchoring it to a hardware module, which is bolted to the MC stage. The filter module, and similarly all the other modules used to heat sink microwave components in the DR, are made from C10100 OFE copper alloy.

A non-magnetic semi-rigid coaxial cable EZ 86-Cu-TP/M17 connects the output port of the Marki filter to an SMP 086 connector on the mounting plate; the cable is 18 cm long and enters a magnetic shield from the Amuneal Manufacturing Corporation, type Amumetal 4K (A4K). The access to the shield is through a chimney on the shield lid. The shield, which is thermalized to the MC stage, is characterized by a DC relative magnetic permeability close to 80000 at 4 K. The SMP 086 connector is mated to the input port of the DUT shown schematically in Fig. 8 of the main text. The DUT used in the DR features SMP 047 connectors in lieu of SMA connectors. The DUT when connected to the horizontal mounting plate is shown in Figs. 1 (d) and 4 (c) of the main text.

The output port of the DUT is then connected to a series of two cryogenic circulators from Raditek Inc., model RADC-4.0-8.0-Cryo-4-77K-S3-1WR-b (with CryoPerm magnetic shielding) by means of a semi-rigid superconducting coaxial cable from Coax Co., model SC-219/50-Nb-Nb, of length 17.3 cm. The circulators are thermalized to the MC stage and are connected to each other by means of a semi-rigid superconducting coaxial cable from Coax Co., model SC-219/50-Nb-Nb, of length 20.7 cm; the spare port of each circulator is terminated with an XMA cryogenic 50 Ω load, model 2001-7010-02-CRYO, which is thermalized to the MC stage. The output port of the second circulator is connected by way of a 51.9 cm long SC-219/50-Nb-Nb cable to a third circulator at the still stage (the spare port is terminated with a 50 Ω load thermalized to the still). A 42.7 cm long SC-219/50-Nb-Nb cable connects the output port of the

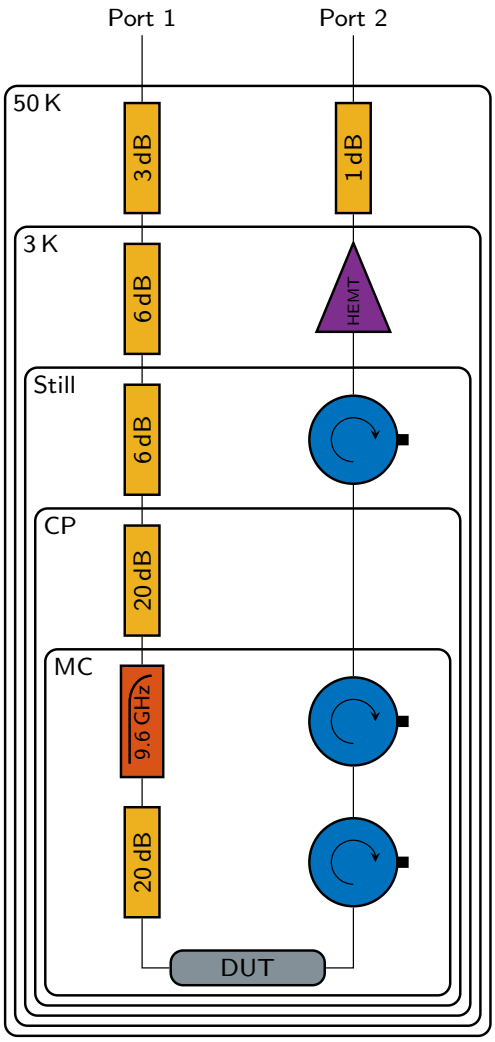

FIG. S1. DR setup. Infrared radiation shields [2, 3] and magnetic shields are used, but not shown.

third circulator to a cryogenic microwave amplifier from Low Noise Factory AB, model LNF-LNC1_12A. The amplifier, which is thermalized to the 3 K stage, is characterized by a nominal gain of approximately 39 dB and a noise temperature of 5 K at an operating temperature of 12 K in the 4 GHz to 8 GHz frequency range. Finally, the amplifier output port is connected to the 50 K and RT stages by a series of two SC-219/50-SS-SS cables of length 38.6 cm and 31.2 cm, respectively; the cables are thermalized to the 50 K stage by means of a 1 dB XMA attenuator. Two EZ Form copper cables in series, followed by SucoFlex flexible cables, complete the network to port 2.

The input channel described here is one of three equivalent channels dedicated to resonator measurements. The three channels share the output line; this is possible thanks to a microwave switch from Radiall, model R573.423.605, which is operated at the MC stage. The switch is located after the DUT, but before the two MC circulators (two of the three input channels and the switch are not shown in Fig. S1). The switch has six inputs and one output, making it possible to further extend the number of input microwave channels.

The S-parameters for resonators $i = 1, 2, \ldots, 5$ were measured with the PNA-X N5242A input power set to 10 dBm, corresponding to $P_{\rm in} = 10\,\mu$W. Considering that the input channel total attenuation at room temperature is $\sim$ 76 dB at 5 GHz, corresponding to $\alpha \simeq 3.98 \times 10^7$, the input power at the resonator is $P'_{\rm in} \simeq 251.3$ pW or -66 dBm. Using this power value in Eq. (4) of the main text, for example, gives the mean photon number $\langle n_{\rm ph}\rangle$ for resonator 2 reported in the main text. The room temperature total attenuation α of the input channel was estimated from the cables' geometry and electrical resistivity and from the nominal value of the XMA attenuators. Note that the resistivity of SUS304 [4] as well as the XMA attenuation values vary only marginally at low temperature and, thus, the room temperature estimate of α can also be used for the DR at operating conditions; the estimate of α for the DR at operating conditions was further confirmed by means of a Planck spectroscopy experiment, as in Ref. [5]. The same value of α was also used when determining the mean photon number $\langle n_{\rm ph}\rangle$ on the horizontal axis of Fig. 16 (resonator 6) in the main text.

S3. ANIMATED ELECTRIC FIELD SIMULATIONS

The electric fields discussed in Subsec. II D of the main text were generated for multiple phases, enabling a time-domain analysis. This made it possible to better visualize the behavior of the simulated fields associated with the various components of the quantum socket. The time-domain animations of the simulated electric field for the three-dimensional wire, the 90° transition between the wire and the on-chip pad, and the first box mode are shown in Movies S1, S2, and S3, respectively.

The simulation of the three-dimensional wire shows a clear impact to the electric field at the dielectric spacers, giving an indication of where potential future improvements of the wire should focus.

The simulation of the 90° transition reveals a surprisingly clean transmission, with no immediately apparent regions of poor performance. The broad field distribution below the contact pad does suggest the appearance of a stray capacitance to the cavity below. However, the TDR results in Subsec. IV C indicate that such a capacitance must be small because of a very good impedance matching at the transition region.

The box mode animation shows the "pinching" effect to the electric field caused by the metallic pillar, leading to a significantly higher relative electric permittivity and, in turn, a much lower frequency of the first box mode ($\sim$6.3 GHz). Some other regions of interest in Movie S3 are the outer edges of the chip recess, where the field be-

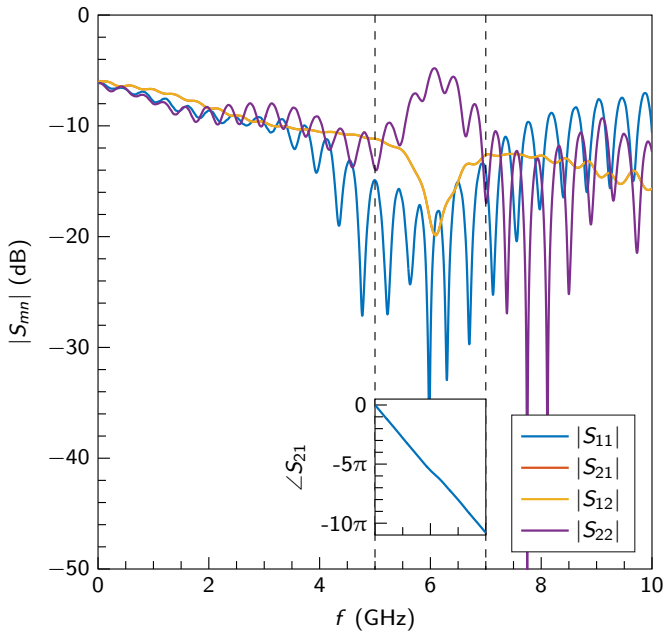

FIG. S2. S-parameter measurements for the Au sample at room temperature in the case of a slightly loose screw-in micro connector. The inset shows the unwrapped phase angle $\angle S_{21}$; the black dashed lines delimit the frequency region between 5 GHz and 7 GHz. The dip at approximately 6 GHz is due to the loose micro-connector.

comes fully confined within the substrate. As the magnitude of the field in this region is quite low, this effect should have only a marginal impact on the performance of the quantum socket. The animation also reveals some field interaction between the box mode and the contact pads (which are characterized by a relatively large area), suggesting these as the main reason for any spurious coupling between on-chip structures and the box modes.

S4. SCREW-IN MICRO CONNECTOR ANOMALY

In order to gain further insight into the electrical behavior of the screw-in micro connector, we report here a set of room temperature measurements showing the appearance of a microwave anomaly associated with the micro connector. These measurements complement the discussion associated with Fig. 9 (b) in Subsec. IV B of the main text.

Figure S2 shows the magnitude and unwrapped phase angle of the S-parameters as a function of frequency for an Au sample in the case of a slightly loose screw-in micro connector; the measurement was performed at room temperature (cf. Subsec. IV B in the main text for details on the DUT used for these measurements). The microwave dip is centered at approximately 6 GHz and has a 3 dB bandwidth of approximately 400 MHz. The dip is likely not a Lorentzian-type feature due to a resonance mode in the package. This is clearly demonstrated by the phase angle of the coefficients S_{21} and S_{12}, which has the characteristic frequency dependence of a transmission line (i.e., no phase shift associated with a resonance). Note that a similar behavior is encountered when performing a microwave measurement with, e.g., a not well torqued SMA connector. As expected from energy conservation, the dip in S_{21} corresponds to a peak in S_{11}; however, the absence of a peak in S_{22} indicates that only the micro connector at the DUT input line was loose in this instance. As explained in the main text, curing the dip at room temperature is rather straightforward. However, it is much harder at low temperatures. Hence, we decided to cool down a DUT without curing the dip that appeared at room temperature. A set of data at 77 K was taken immediately after the room temperature data, as shown in Fig. 9 (b) in Subsec. IV B of the main text. We monitored the S-parameters throughout the cooldown, observing how the dip shifted from approximately 6 GHz to 2 GHz while cooling. It is reasonable to assume that, when cooling down, the micro connector became looser due to thermal contractions, thus giving rise to a microwave transmission dip at lower frequency.

S5. SUPERCONDUCTING RESONATORS COUPLING AND FIT

Figure S3 shows a detail of the coupling region between one of the CPW transmission lines and a $\lambda/4$-wave resonator shown in Fig. 14 of the main text. The width and gap of the CPW transmission line are indicated. The resonator center conductor width W and dielectric gap G are also indicated, as well as the coupling length ℓ_κ and the line-resonator ground separation (5 µm); note that the line-resonator ground separation for resonator 6 is 20 µm. The length ℓ_κ determines how strongly the resonator is coupled to the transmission line and, thus, the resonator rescaled coupling (external) Q_c^* quality factor [6, 7].

Figure S4 shows a polar plot of the real and imaginary part of the normalized inverse transmission coefficient $\tilde{S}_{21}^{-1}$ of the data shown in Fig. 15 (d) of the main text, along with the fit. The equation used for the fit

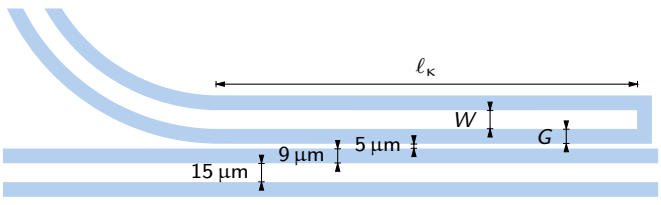

FIG. S3. Coupling region between a CPW transmission line and a $\lambda/4$-wave resonator. White surfaces represent conductive material and blue surfaces dielectrics (Si or sapphire).

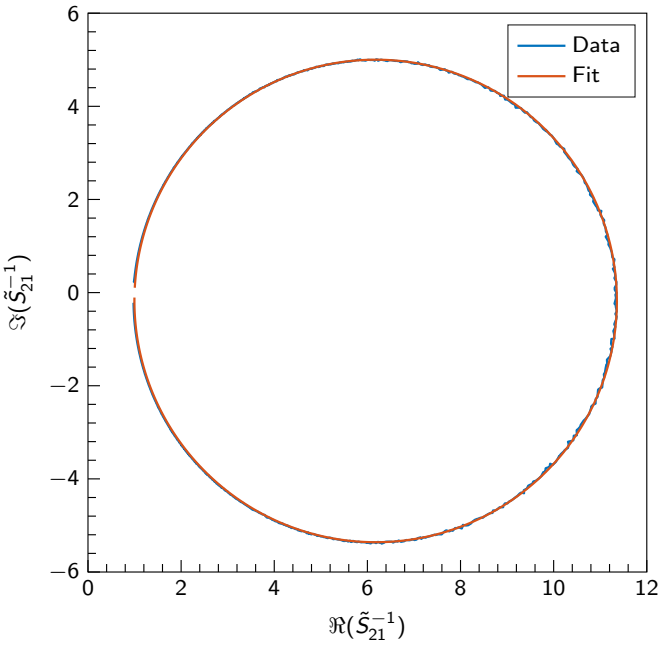

FIG. S4. Polar plot of the normalized inverse transmission coefficient $\tilde{S}_{21}^{-1}$ for superconducting resonator 2 discussed in the main text. Data in blue and fit from Eq. (S1) in red.

is [7]

$$\tilde{S}_{21}^{-1} = 1 + \frac{Q_\mathrm{i}}{Q_\mathrm{c}^*} e^{i\phi} \frac{1}{1 + i2Q_\mathrm{i}\delta x} \quad , \tag{S1}$$

where ϕ is an offset angle, $\delta x = (f - f_0)/f_0$, and $i^2 = -1$ is the imaginary unit. A normalization is applied before the fit to set the off-resonance transmission magnitude and phase to 0 dB and 0 rad, respectively. The fit parameters for the resonator in Fig. 15 (d), i.e., resonator 2, of the main text were found to be $f_0 = 5\,064\,513\,933(6)$ Hz, $Q_\mathrm{c}^* = 16002(4)$, $Q_\mathrm{i} = 165790(60)$, and $\phi = -0.0347(3)$.

S6. SPRING TESTS

As discussed in Appendix D of the main text, Movie S4 shows the setup used to test the springs at low temperature. In the movie, two springs mounted in series are compressed, after having been submerged in liquid helium. This process was repeated multiple times, without any damage occurring to the spring or any measurable change in the spring constant. The same setup also made it possible to preform compression measurements while the springs were submerged in a cryogenic liquid (nitrogen or helium); the compressive force was applied at the top of the rod, which always remained at room temperature.

S7. HIGH/LOW-TONE QUBIT MEASUREMENT

Figure S5 shows an extended version of the surface code architecture in Fig. 17 of the main text. In panel (a), numbers from 0 to 5 represent arbitrary frequencies (tones) from low to high (0 means a lower frequency than the others). Every qubit is coupled to two measurement resonators; note that label 0 is associated with a CPW transmission line that is coupled to a set

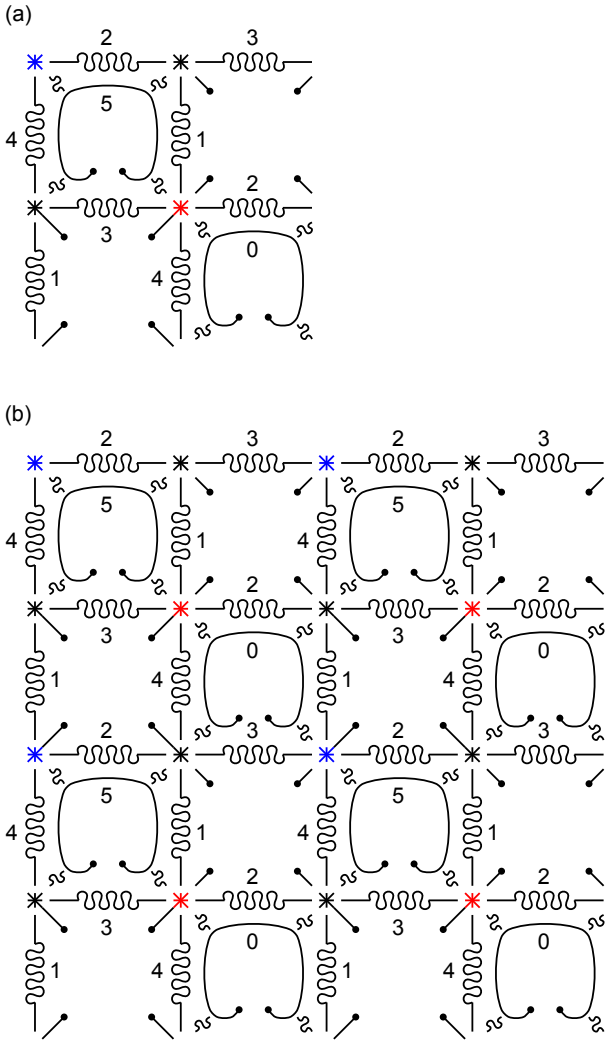

FIG. S5. Extended surface code architecture compatible with the quantum socket. (a) The main difference compared to the architecture presented in the main text is the addition of an extra measurement resonator for each qubit. In this case, the qubits are named *octatons* due to their eight arms. The various frequencies (tones) from low to high are indicated by the numbers $0, 1, 2, 3, 4$, and 5, respectively. The CZ gates follow the same numeration [8]. Measurement qubits are indicated in red and blue and data qubits in black. (b) Larger portion of the two-dimensional lattice.

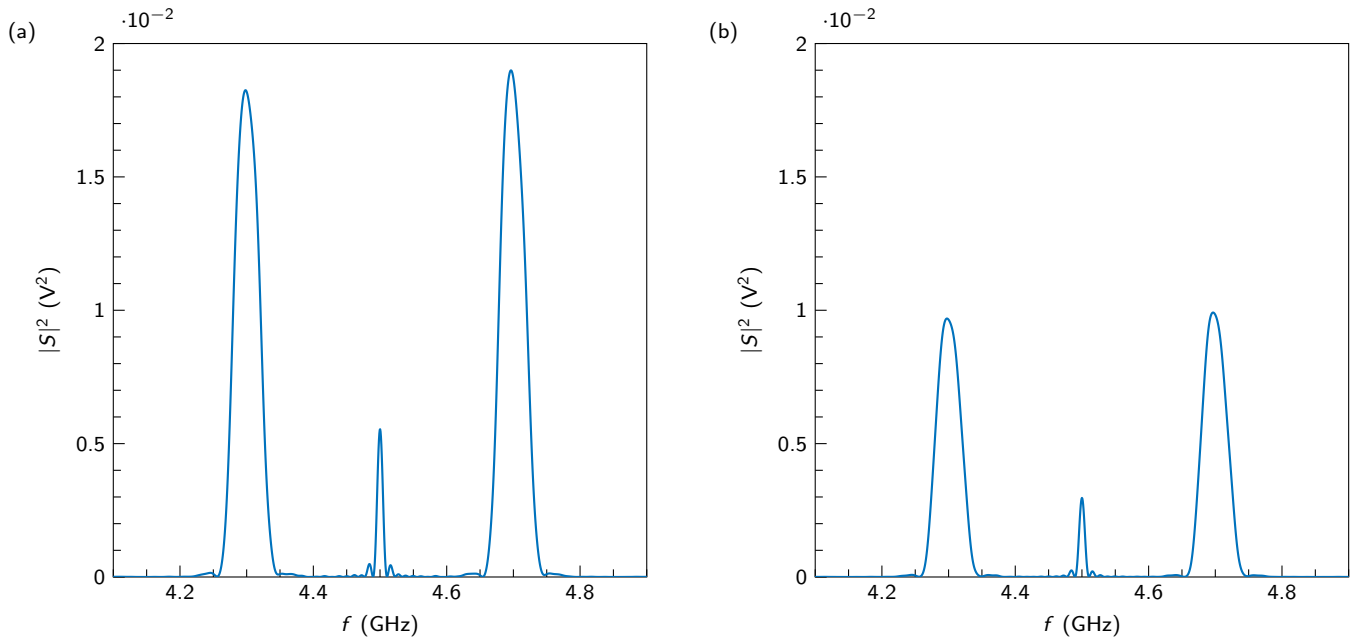

FIG. S6. Magnitude as a function of frequency of a Fourier-transformed pulsed signal. (a) Pulse transmitted through a reference flexible coaxial cable. (b) Similar pulse transmitted through a quantum socket.

of four measurement resonators, all at slightly different frequencies (to allow multiplexing) centered around frequency 0. Similarly, label 5 is associated with a CPW transmission line that is coupled to a set of four measurement resonators, all at slightly different frequencies centered around frequency 5. In this architecture, all qubits start at a low frequency and then increase in frequency in unison to perform two-qubit CZ gates through the coupling resonators in the correct sequence; in the figure, this sequence is indicated by the labels (coupling frequencies) $1, 2, 3$, and 4. One-qubit gates can be applied when and if required. Finally, the measurement qubits (red and blue) are readout at frequency 5. This is one surface code cycle [8]. The process is then reversed and during the downward uniform frequency sweep, again, an appropriate sequence of CZ gates is executed, followed by readout at frequency 0, implementing the next cycle. This process avoids sweeping either measurement or data qubits past resonators during the cycles. Panel (b) shows a larger portion of the surface code lattice. The lattice is compatible with the quantum socket introduced in this work.

S8. MICROWAVE PULSE TRANSMISSION

In Appendix G of the main text, we have shown that the quantum socket is characterized by a small frequency dispersion. In this section, we describe a set of experiments, where actual fast microwave pulses were applied to the quantum socket as well as a reference cable. This makes it possible to assess the effects of dispersion directly on pulses similar to those to be used for the manipulation of superconducting qubits.

Figure S6 shows the magnitude of the Fourier transform of a pulse transmitted through the reference cable (panel (a)) and a quantum socket (panel (b)), both at room temperature. The pulse was generated by mixing a sinusoidal carrier signal at 4.5 GHz with a Gaussian-modulated sinusoidal pulse at 200 MHz. The time length of the Gaussian envelope was 15 ns (full width at half maximum (FWHM)). The carrier signal was generated by means of a microwave source from Keysight, model E8257D PSG; the mixer was an in-phase and quadrature (IQ) mixer from Marki, model IQ-0307LXP; the IQ components of the modulated Gaussian were generated by means of a customized low-noise arbitrary waveform generator (AWG) from Tabor Electronics Ltd., model WX2184C+; all instruments were synchronized by way of a rubidium atomic timebase part of a digital delay generator from Stanford Research Systems, Inc., model DG645/15, which was also used to trigger the AWG through an SRD1 module from Stanford Research Systems as well. The generated signal was split by way of a microwave power divider from Krytar, Inc., model 6005180, with one output sent through a reference SucoFlex flexible coaxial cable from Huber+Suhner of length 1.5 m and the other output through the quantum socket (DUT of Fig. 8 in the main text). The output of each path was acquired and digitized using a real-time oscilloscope from Keysight, model DSO91204A, also synchronized with the rubidium timebase. The pulse going through the quantum socket is attenuated due to the resistance of the Ag CPW transmission line, hence, the

magnitude of the Fourier transform is lower than of the reference signal. However, the overall shape of the two pulses is very similar, with marginal distortions.

[1] Rami Barends, Julian Kelly, Anthony Megrant, Daniel Sank, Evan Jeffrey, Yu Chen, Yi Yin, Ben Chiaro, Josh Mutus, Charles Neill, Peter O'Malley, Pedram Roushan, James Wenner, Theodor C. White, Aandrew N. Cleland, and John M. Martinis, "Coherent josephson qubit suitable for scalable quantum integrated circuits," Phys. Rev. Lett. **111**, 080502 (2013).

[2] Rami Barends, James Wenner, Michael Lenander, Yu Chen, Radoslaw C. Bialczak, Julian Kelly, Erik Lucero, Peter O'Malley, Matteo Mariantoni, Daniel Sank, Haohua Wang, Theodor C. White, Yi Yin, Jian Zhao, Andrew N. Cleland, John M. Martinis, and J. J. A. Baselmans, "Minimizing quasiparticle generation from stray infrared light in superconducting quantum circuits," Appl. Phys. Lett. **99**, 113507 (2011).

[3] Antonio D. Córcoles, Jerry M. Chow, Jay M. Gambetta, Chad Rigetti, James R. Rozen, George A. Keefe, Mary B. Rothwell, Mark B. Ketchen, and Matthias Steffen, "Protecting superconducting qubits from radiation," Appl. Phys. Lett. **99**, 181906 (2011).

[4] Patxi Duthil, "Material properties at low temperature," in *Proceedings of the CASCERN Accelerator School: Superconductivity for Accelerators, Erice, Italy, 24 April 4 May 2013*, Vol. CERN-2014-005 (CERN, Geneva, 2014), edited by Roger Bailey (2014) pp. 77–95.

[5] Matteo Mariantoni, Edwin P. Menzel, Frank Deppe, Miguel Á. Araque Caballero, Alexander Baust, Thomas Niemczyk, Elisabeth Hoffmann, Enrique Solano, Achim Marx, and Rudolf Gross, "Planck spectroscopy and quantum noise of microwave beam splitters," Phys. Rev. Lett. **105**, 133601 (2010).

[6] Luigi Frunzio, Andreas Wallraff, David Schuster, Johannes Majer, and Robert Schoelkopf, "Fabrication and characterization of superconducting circuit QED devices for quantum computation," IEEE Trans. Appl. Supercond. **15**, 860–863 (2005).

[7] Anthony Megrant, Charles Neill, Rami Barends, Ben Chiaro, Yu Chen, Ludwig Feigl, Julian Kelly, Erik Lucero, Matteo Mariantoni, Peter J.J. O'Malley, Danial Sank, Amit Vainsencher, James Wenner, Theodor C. White, Yi Yin, Jian Zhao, Christopher J. Palmstrøm, John M. Martinis, and Andrew N. Cleland, "Planar superconducting resonators with internal quality factors above one million," Appl. Phys. Lett. **100**, 113510 (2012).

[8] Austin G. Fowler, Matteo Mariantoni, John M. Martinis, and Andrew N. Cleland, "Surface codes: Towards practical large-scale quantum computation," Phys. Rev. A **86**, 032324 (2012).